MTLA 40 (2025) 102417

Contents lists available at ScienceDirect

Materialia

journal homepage: www.elsevier.com/locate/mtla

Beyond transmission electron microscopy imaging: Atom probe tomography reveals chemical inhomogeneity at stacking fault interfaces in InGaN/GaN light-emitting diodes

Ruiying Shu [a,*], Rachel A. Oliver [b], Martin Frentrup [b], Menno J. Kappers [b], Huixin Xiu [b,c], Gunnar Kusch [b], David J. Wallis [b,d], Christina Hofer [a], Paul A.J. Bagot [a], Michael P. Moody [a]

[a] Department of Materials, University of Oxford, Parks Road, Oxford OX1 3PH, UK
[b] Department of Materials Science and Metallurgy, University of Cambridge, 27 Charles Babbage Road, Cambridge CB3 0FS, UK
[c] Present address: School of Materials and Chemistry, University of Shanghai for Science and Technology, 516 Jungong Road, Yangpu District, Shanghai 200093, China
[d] Centre for High Frequency Engineering, University of Cardiff, 5 The Parade, Newport Road, Cardiff CF24 3AA, UK

ARTICLE INFO

Keywords:
Gallium Nitride (GaN)
Atom Probe Tomography (APT)
Stacking Fault (SF)
Light-emitting Diode (LED)
Zincblende (zb)
Quantum Wells (QWs)

ABSTRACT

In this study, we present an atom probe tomography investigation of zincblende InGaN-based multi-quantum well light-emitting diode (LED) structures with a specific focus on the influence of stacking faults within the system. We demonstrate that the visualisation of stacking faults in atom probe reconstructions is possible due to previously documented sensitivities of measured composition in III-V materials to local variations in electric field during the experiment. Meanwhile, we quantify the composition of indium (In) in the InGaN quantum wells and establish that elongated regions exist, parallel to ridges on the sample surface, in which the indium content is increased. We discuss this observation in the context of previous scanning transmission electron microscopy (STEM) data which suggested that such In rich regions are associated with stacking faults. Our experiments not only showcase the feasibility of stacking fault characterization in InGaN-based multi-quantum well LEDs through atom probe tomography (APT) but also offer a practical pathway towards three-dimensional imaging and compositional analysis of stacking faults at the atomic scale.

1. Introduction

III-nitride light-emitting diodes (LEDs) have revolutionised the field of optoelectronics [1,2]. InGaN alloys have a direct, tuneable bandgap, providing opportunities for the fabrication of LEDs across the visible spectrum, and also have relevance to photo-detectors and lasers [3,4]. Solid state lighting is reliant on highly efficient blue LEDs, which are then down-converted to other wavelengths using phosphors [5–7]. Such down-converted blue emitters are used in preference to incorporating separate red, green, and blue LEDs and avoiding down-conversion. This preference is largely due to the considerably lower efficiency observed in green emitters, a phenomenon known as the ‘green gap’ that persists even today [8–14]. Furthermore, as technologies for micro-displays develop, there is increasing demand for red, green, and blue nitride micro-LEDs based on the expectation that they can be used to achieve a long lifetime, low energy consumption, high resolution, and wide colour gamut with high purity [15,16]. Here again, the lower efficiency of longer wavelength devices motivates attempts to improve their performance.

To address these challenges, researchers are now exploring zincblende (zb) InGaN-based emitters as an alternative to conventional devices based on the wurtzite structure [17]. The zb-nitrides have been suggested to offer a route to more efficient green emission because, for samples grown in the (001) orientation, piezoelectric and spontaneous polarisation fields which reduce the rate of radiative recombination in wurtzite nitrides can be avoided. Furthermore, zb-nitrides have a smaller bandgap than their wurtzite counterparts [18]. We note that the application of zb-InGaN in green-emitting LEDs will also be impacted by the bandgap bowing parameter, the value of which remains a subject of some discussion [19]. However, intrinsic {111} stacking faults (SFs) are commonly found in zincblende nitrides [20]. These extended planar defects may lead to local variations in Indium content in the quantum wells (QWs), potentially reducing the spectral purity and influencing device efficiency [21,22]. The impact of SFs on devices fabricated using

---

* Corresponding author.
E-mail address: ruiying.shu@materials.ox.ac.uk (R. Shu).

https://doi.org/10.1016/j.mtla.2025.102417
Received 21 February 2025; Accepted 22 April 2025

this alternative nitride crystal structure is still relatively unexplored, and further characterisation of their structure and composition can help us understand how they influence the performance of LEDs.

Previous studies have provided valuable insights into the impact of SFs on materials properties and their potential role in device performance. Ding et al. used energy-dispersive X-ray spectroscopy (EDS) in the scanning transmission electron microscope (STEM) to investigate compositional variations arising adjacent to SFs in a zb-nitride LED structure containing InGaN QWs and an AlGaN electron blocking layer (EBL) [22]. They found that both In in the quantum well region and Al in the AlGaN layer showed SF-related segregation effects, although In tended to segregate adjacent to the SFs, whilst Al segregated directly on the SF. Also, they interpreted the In segregation as being related to quantum wires (QWires); however, their images do not directly show elongated wire-like features, but rather a 2D projection which they suggested to correspond to a wire-like feature viewed end on, with the quantum wire running through the thin foil parallel to the viewing direction. Hence, further evidence for the formation of wire-like features is needed and data on their size, shape, and composition is desirable. This is particularly interesting since Church et al. showed that samples containing In segregation adjacent to stacking faults also show a high degree of linear polarisation in the emission from the QWs, and attributed that polarisation to the postulated QWire structures since the In-rich region adjacent to the SF is expected to lead to a locally reduced bandgap [23]. Therefore, further detailed 3D characterization of the postulated QWires is required and atom probe tomography (APT) is one valuable option for such studies.

As a powerful tool for studying materials at the atomic scale in three dimensions, APT offers high spatial resolution and chemical sensitivity. APT analyses are enabled by applying a large electrical field to a needle-shaped specimen tip that ionizes and pulls the atoms off the tip's surface one-by-one, i.e., field evaporation [24]. The type and position of the ionized atoms are determined using time-of-flight mass spectrometry, a position-sensitive detector, and a 3D reconstruction model [25]. In this way, it offers 3D chemical mapping at the atomic scale, providing invaluable insights into material composition and elemental distribution. However, APT is limited in providing detailed crystallographic structure information, such as specific plane orientations. To address this limitation, STEM often plays an important role of complement with its high-resolution visualization of nanoscale crystal structures, which can be seen in previous studies that have successfully combined STEM with APT to enhance the overall understanding of material properties [22,26–31]. A representative example is the study by Mancini et al. [32], where both STEM and APT were applied to investigate In enrichment associated with SFs in wurtzite InGaN QWs. While their work revealed compositional inhomogeneities correlated with structural defects, a comprehensive interpretation was limited, which is potentially due to uncertainties in the identification of crystal orientation in the APT experiment.

In our study, a combination of APT and STEM was used to investigate the atomic-scale compositional variation within InGaN QWs and the commonly occurring SFs in zb III-nitrides. Specifically, the operational parameters of APT were optimized, with a particular focus on their effect on quantitative measurements. Meanwhile, due to structural variations in the SF region resulting in different evaporation fields during APT measurement, this technique has proven capable of imaging the SFs without the need for any compositional segregation to highlight the structure. In addition, the chemical composition of the SFs and their surrounding regions have been investigated, providing insights into their formation mechanisms that will facilitate future studies of their effects on emitter performance.

2. Materials and methods

2.1. Zincblende GaN

The zincblende (zb) InGaN-based multi-quantum well (MQW) LED structure investigated in this study was the same as that described in reference [22]. The zb-GaN heterostructure was grown using metal-organic vapour phase epitaxy (MOVPE) inside a 6 × 2-inch close-coupled showerhead reactor from Thomas Swan. The sample was prepared using a 20 × 20 mm^2 section of a 150 mm diameter 3C-SiC/Si substrate (supplied by Kubos Semiconductors Ltd). This substrate is composed of a ≈ 3 μm thick layer of 3C-SiC grown on a 1000 μm thick Si (001) substrate with a 4° miscut towards one of the ⟨110⟩ in-plane directions. The nitride epitaxial layers consist of a 460 nm thick Si-doped GaN layer, an active region consisting of five InGaN quantum well (QW) layers with a thickness of 3 nm each, alternating with 11 nm GaN barriers, a 10 nm undoped GaN layer, a 15 nm AlGaN EBL doped with magnesium and a 180 nm p-GaN cap layer doped with magnesium. Previous investigations of this structure using STEM [22,33], reveal stacking fault densities typical of MOVPE-grown zb GaN, which (based on quantitative analysis of comparable material [34] are likely to be in the 10^5cm^{-1} regime. Note cathodoluminescence spectroscopy on this sample reveals QW luminescence at 2.71 eV [33].

2.2. STEM

Cross-sectional samples were prepared for scanning transmission electron microscopy (STEM), using an *in-situ* lift-out method in a FEI Helios NanoLabTM focussed ion beam (FIB). Initial STEM studies were then performed in a FEI Tecnai Osiris. Atomic resolution STEM annular bright field (ABF) and high angle annular dark field (HAADF) images later were acquired simultaneously in a Thermo Fisher ScientificTM Titan Themis Probe-corrected STEM. Sample preparation details and imaging conditions for the two STEM experiments can be found in references [22] and [35] respectively.

2.3. APT

Needle-shaped APT specimens with tip diameters <100 nm were prepared using a Zeiss Crossbeam 540 Analytical Focused Ion Beam/Scanning Electron Microscope (FIB-SEM). Prior to milling with the FIB, a protective layer of platinum was deposited on the area of interest (2 μm × 20 μm, 30 kV, 100 pA). The triangular cross-section wedge beneath the platinum rectangle was milled on three faces, employing a voltage of 30 kV and a current ranging from 1.5 nA to 300 pA. For undercut milling, a current of 300 pA was used near the protective layer. In the lift-out process, an in-situ micromanipulator was employed to approach one side of the wedge, maintaining a small gap with the sample. Subsequently, platinum was deposited to the junction of the wedge and the nanomanipulator for soldering (30 kV, 50 pA) and then cut from the other side (30 kV, 300 pA). Subsequently, 1.5 μm to 2 μm wide segments were mounted sequentially onto standard Si column microarrays (Cameca Instruments) and then separated from the wedge-shaped segments by milling (30 kV, 300 pA). Each segment was individually shaped into needles using a sequential annular milling pattern with decreasing inner diameters. Since the material is very sensitive to the ion beam [36], the sharpening process needs to be very careful. The process began at 30 kV and 300 pA, reducing the needle diameter to approximately 1 μm. Then the parameters were adjusted to 30 kV and 100 pA to further sharpen the needles to about 200 nm to 300 nm. A final refinement step was performed at 30 kV and 10 pA, reducing the diameter to <100 nm. To minimize milling damage, a treatment at 2 kV and 10 pA was applied during the last stage of sharpening. Careful polishing was then performed to remove the remaining platinum protective layer while retaining the near-surface layers of interest.

These specimens were then transferred to a direct flight path

CAMECA LEAP 5000 XS under non-vacuum ambient conditions at room temperature and atmospheric pressure. Atom probe measurements were performed at a cryogenic temperature of 50 K, using a pulsed laser (333 kHz to 500 kHz, 0.03 pJ to 10 pJ per pulse). Multiple APT datasets were obtained from various APT tips at different laser energies (0.03 pJ to 10 pJ per pulse). The APT datasets were analysed using the commercial software packages IVAS 6.3 and AP Suite 6.1

3. Results and discussion

3.1. Visualization of atomic structures with STEM

An overview image of the full GaN epitaxial structure as viewed in STEM is shown in Fig. 1(a). SFs are observed extending from the GaN/SiC interface through all the layers in the sample, and are seen to occur in two orientations, which incline towards one another. As discussed elsewhere, for SFs viewed perpendicular to the sample miscut, one set of SFs is at a shallower angle (51°) and the other at a steeper angle (59°) with respect to the GaN/SiC interface [34]. Oppositely inclined SFs can meet and annihilate one another [34], but, a substantial proportion of the SFs extends through the material, reaching the surface of the sample.

We have examined the detailed structure of SFs in a sample very similar to the GaN buffer which underlies the MQW region in the LED structure. This sample is described in detail in [35] where we discuss the imaging technique required to visualise not only the heavier Ga atoms, but also the lighter N atoms. Following the approach used in that work, Fig. 1(b) shows the result of merging an Annular Bright Field (ABF) image and a High Angle Annular Dark Field (HAADF) image of the zb-GaN (zone axis = [110]), so that Gallium (Ga) atomic columns appear as green circles, whilst Nitrogen (N) atomic columns appear as smaller dark dots, against a red background.

The region of zb-GaN examined here contains two intersecting SFs, which can be initially identified by considering the stacking sequence on the Ga sub-lattice. The stacking sequence is labelled on the figure, and at the faults, we observe a change from ABCABC stacking to ABC-AB-ABC, consistent with the expected structure of I1 SFs. We also note that directly at the I-SF plane (depicted by the white dashed line) the coordination of the N-atoms is rotated by 180° around the polar axis along [1-11], consistent with our previous observations. A key point of note for comparison with APT data that we will present later is that in this case the two SFs intersect one another but both propagate unimpeded through the crystal structure. This implies that the Burgers vectors of the SFs are such that SF annihilation is energetically unfavourable in this case [34].

3.2. APT reconstruction

After conducting an analysis of various APT samples, we were able to achieve a high success rate in producing valid data without encountering tip fractures during the experiment. Data volumes ranging from 35 million to 75 million ions on different samples were successfully collected.

An example of a zb-GaN reconstruction is presented in Fig. 2, which shows 73 million ranged ions detected using a pulse energy of 10 pJ. Characteristic elements such as Gallium (Ga), Nitrogen (N), Indium (In) and Aluminium (Al) were successfully collected. The APT 3D reconstruction in Fig. 2 showcases a relatively uniform distribution of Ga and N. Additionally, the active layer region contains distinct layers of In-containing material, and these InGaN layers directly correspond to the expected positions of the QWs. The AlGaN layer was also clearly imaged using APT. The reconstructions indicate the successful collection of the QWs and the AlGaN layer in the zb-GaN LED structure.

Although the QWs and AlGaN layers are visible, they are not flat and oriented parallel to one another other like the planar layers usually observed in APT analysis of LED structures grown from the more conventional wurtzite form of GaN. Some angular differences between the QW layers and between the QWs and the Al layers can be readily seen in the Fig. 2. This is consistent with the STEM data in Fig. 1(a) and in Ding et al. [22] which show changes in orientation of the QWs, some of which may be associated with SFs.

3.3. APT analysis of SFs within the InGaN/GaN based LED

Further investigation revealed that the observed Ga distribution is not always uniform. In the dataset collected at 500fJ, as shown in Fig. 3, an uneven distribution of Ga is clearly visible in the lower section of the APT reconstruction. Shown in Fig. 3(a), the Ga iso-concentration surfaces highlight an apparently inhomogeneous distribution of Ga and reveal the presence of straight, planar features. These planar Ga iso-concentration surfaces intersect at an approximate 70°angle corresponding to the expected angle of two intersecting {111} planes and to the angles at which the two SFs intersect one another in the STEM image in Fig. 1(b). Notably, this spatial reconstruction of the APT data was first calibrated using QW spacings, revealing an apparent angle of approximately 70°. Based on this, a further recalibration was performed to achieve an improved match between the angle observed in the dataset and the expected angle between intersecting SFs while maintaining the QW spacings observed in the TEM data [22]. Consequently, the reconstructed planar Ga iso-concentration surfaces in the dataset displayed in Fig. 3 now intersect very close to 70°. A one-dimensional concentration profile is plotted along the length of the red arrow in Fig. 3(a) (region of

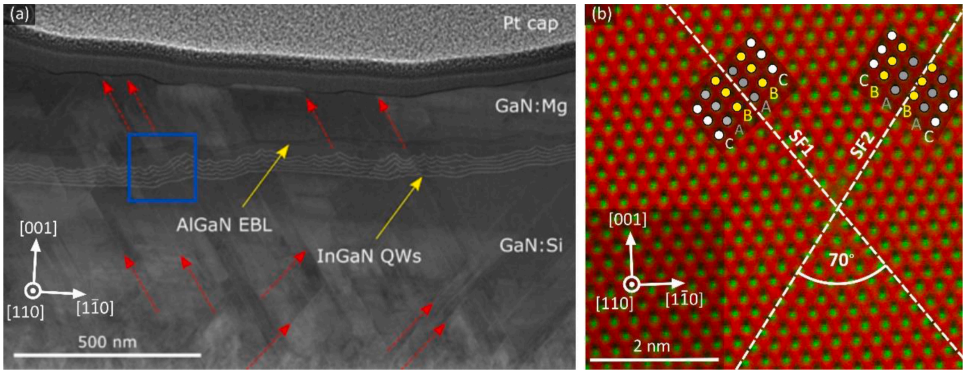

Fig. 1. (a) HAADF STEM image of an overview of a zincblende GaN sample. The red dashed arrows represent SFs. The blue box highlights a region of the five-layer quantum well (QW) structure. From Ding, B. *et al.*, "Alloy segregation at stacking faults in zincblende GaN heterostructures." *Journal of Applied Physics*, 2020, Vol. 128, Issue 14, Pages 145,703. DOI: 10.1063/5.0015157. This image is licensed under the Creative Commons CC BY license. (b) RG mixture of ABF and HAADF images. The large green dots represent Ga, and the small dark ones correspond to N. The white dashed lines illustrate two intrinsic SFs, with the blue, yellow, and white dots indicate the atomic columns with stacking type of -A-, -B-, and -C-, respectively.

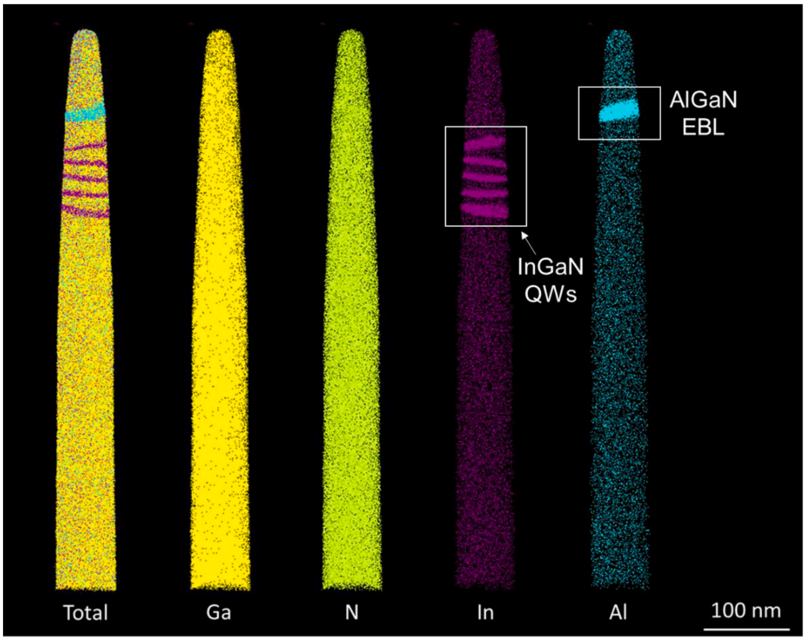

Fig. 2. Atom maps for gallium (Ga), nitrogen (N), indium (In), aluminium (Al) and illustrating the presence of 5 InGaN QWs and the AlGaN EBL. A representative mass spectrum is provided in Supplementary Fig.

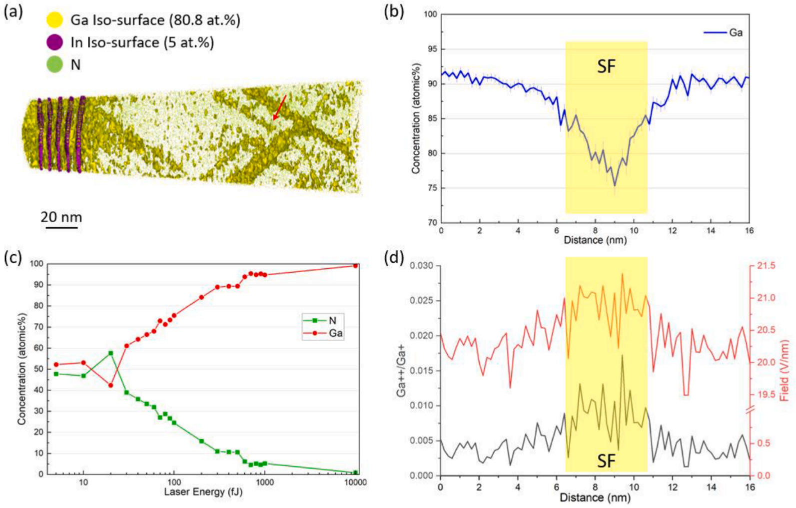

Fig. 3. (a) APT reconstruction of InGaN/GaN MQW LED containing SFs. The yellow iso-concentration surfaces on the right indicate the SFs. The red arrow is aligned perpendicular to the SF plane. (b) One-dimensional concentration distribution of Ga in the volume (10 nm × 30 nm × 20 nm) along the red arrow in (a), the yellow-coloured area corresponds to the SF region. (c) Concentration profile of wurtzite GaN collected by APT at different laser energies. (d) Charge-state ratio of Ga^{2+}/Ga^{+} as a function of distance along the direction of the red arrow in (a) (left axis). The corresponding evaporation field (right axis). The Yellow-coloured area corresponds to the SF region.

interest of 10 nm × 30 nm × 30 nm), orientated perpendicular to the plane. As shown in Fig. 3(b), it is evident that the Ga concentration shows a sharp decrease across the suspected SF region compared to the adjacent bulk region.

However, as a partially ionic crystal, GaN does not tolerate significant deviations from stoichiometry. Furthermore, the TEM data in Fig. 2 does not show a deviation in the intensity of the atomic columns – which might result from a change in the Ga or N content – only a change in their position. Despite the presence of the SF, it is expected that the actual Ga concentration in this region of the material should be the same as in the other parts in the same layer. The reason for the observed inhomogeneity in the region can be attributed to biased evaporation during the APT experiment.

Several APT studies on GaN-based semiconductors in recent years [37–41] have shown that the observed stoichiometry is greatly affected by the analysis conditions, in particular the local electric field applied during the experiment. The instantaneous electric field that was applied to a specific local area of the specimen surface during the experiment can be estimated by measuring the charge state ratio (CSR) of an elemental ionic specie [38] originating from that region and at that time in the analysis. Using this approach, we are able to investigate if it is actually the variation in the local electric field in the vicinity of the SF that causes the change in the concentration we observe.

Fig. 3(c) presents the results from a series of APT calibration experiments with pure wurtzite GaN samples. Here, while maintaining a constant detection efficiency of 1, different laser pulse energies were systematically applied, which in turn corresponds to the application of different electric fields. As expected, the measured composition exhibits significant variability as the laser energy changes. This experiment once again reaffirms the notion that a minor change in the applied electric field strength leads to a measurable change in the concentration measurement by APT in GaN semiconductor materials. For this reason, the measured Ga content of approximately 92 % away from the stacking fault in Fig. 3(b) is a consequence of the phenomenon, not the actual Ga concentration in the sample. As previously observed, the trend in Fig. 3 (c) shows that the lower field strengths are associated with the measurement of an excess of the metallic element, Ga, and its concentration diminishes at higher fields. At lower electric fields (i.e. higher laser energies), this phenomenon is most often attributed to the evaporation and subsequent decomposition of larger complex ions en route to the detector. A potential product of this process is neutral N_2 molecules. These molecules will not be further accelerated towards the detector by the electric field, and thus may lead to a systematic loss in the detection of nitrogen in the experiment. Although the impact of this phenomenon decreases under higher electric fields, compositional measurements may still exhibit a bias towards the preferential evaporation of gallium. This bias persists irrespective of the applied laser pulse, leading to the erroneous measurement of lower Ga concentrations [42]. This phenomenon has also been found to occur in the APT analysis of other III-V semiconductors and similar effects have also been observed in MgO [43].

Returning to our study of the zb-GaN samples, the change in the Ga^{2+}/Ga^{+} ratio (CSR) across the width of the stacking fault was evaluated. Fig. 3(d) plots the measured CSR and the corresponding estimate of the electric field strength in the same volume and in the same direction as the one-dimensional concentration profile in 3(b), respectively. The electric field strengths were calculated from the CSR using the Kingham curves [44,45]. In the region of the 1D concentration profile where the Ga concentration decreases, there is a significant increase in the field strength. The increase is tentatively attributed to a local change in the apex shape of the specimen, potentially a consequence of the SF intersecting with the surface during the experiment. This supports our previous assumption that there are structural differences in this part of the sample.

In summary, although in reality the overall Ga concentration in the sample is constant, we can still observe compositional fluctuations in the SF region due to variations in field strength caused by crystallographic structural differences. In turn, this enables the observation of SFs by APT.

Having shown that the APT can reveal SFs in the lower section of the sample, we now address whether we can identify their impact on the QW composition within the available data sets. To discuss this, we introduced an additional data set, as shown in Fig. 4, where there are more pronounced phenomena in the InGaN layers. In Fig. 4(a), a three-dimensional reconstruction reveals the spatial distribution of In across the QW layers. It is worth noting that although the QWs exhibit a layered configuration, they deviate from being perfectly parallel planar surfaces. Instead, they appear as a series of near-parallel surfaces undulating up and down, which is consistent with STEM observations as highlighted by the region in the blue box in Fig. 1(a) [22].

It is worth emphasising that, as previously discussed in reference to Fig. 3, the direct quantification of overall composition in Group III-V materials presents challenges, primarily stemming from potential biases related to variances in the evaporation fields of distinct elements. The inaccuracy in N concentration can lead to distorted measurements of the concentrations of the group III elements such as In Previous studies have demonstrated that while there is a bias in the measurement of III:N ratios in this material using APT, there is no observable bias in the measurement of site fractions of the Group III elements, e.g. In/(In+Ga), in InGaN quantum wells (QWs) with random alloy distributions [38,46]. However, a more recent work by Di Russo et al. [47] has suggested that even the Group-III site fraction in InGaN may exhibit a weak dependence on the surface electric field, which is likely due to preferential Ga evaporation under high-field conditions. In the context of our study, where all structures were analysed under consistent experimental parameters, the Group III site fraction remains a reliable measure for assessing local compositional variations. To enhance the precision of our analysis regarding the compositional variations in Group III elements, we will here employ the Group-III site fraction wherever possible to eliminate the bias introduced by local changes in the electric field.

The five images in Fig. 4(b) offer a top-down perspective of the In/(Ga+In) site fraction for each QW, highlighting significant variations in the In content. It appears that each layer exhibits a non-uniform distribution of In, resulting in parallel stripes of high In content seen in plan view. The top section of Fig. 4(c) provides a side view of the third QW depicted in Fig. 4(b) that has been isolated and analysed further. In the

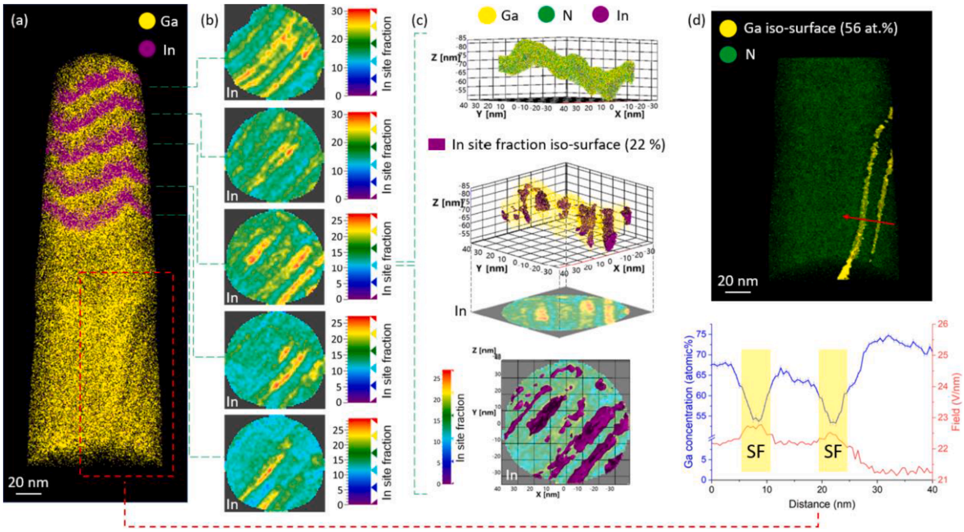

Fig. 4. (a) APT reconstruction containing five QW layers (purple) and a region containing SFs (marked by red dashed box). (b) 2D site fraction map of in each QW in plan view. (c) Top: Side view of the 3rd QW. Middle: In-rich regions in the 3rd QW indicated by purple iso-surfaces (≥22 %). Bottom: Plan view of 2D site fraction map and In site fraction iso-surfaces in the 3rd QW. (d) Top: APT reconstruction showing the GaN region. The yellow concentration iso-surfaces show the SFs. Bottom: Concentration profile of Ga (left axis) and corresponding electric field (right axis) in the volume (20 nm × 20 nm × 40 nm) represented by the red arrow through the SF region in the above figure.

middle section of Fig. 4(c), In site fraction iso-surfaces at 22% In are superposed on a 3D map of the In site. These iso-surfaces enclose the regions of indium-rich material and hence illustrate their elongated shape. This is further emphasised in the bottom section of Fig. 4(c), which shows the iso-surfaces in plan view. The use of iso-surfaces separates the impact of thickness variations and compositional variations in the QW, whereas thickness variations might influence the data visualisations in Fig. 4(b). Hence, Fig. 4(c) allows us to unambiguously identify elongated, wire-like regions of indium enrichment in the QW. To quantitatively assess this In-enrichment, the average In site fractions in both the In-enriched region and the region between the wire-like features have been calculated. The average In site fraction in the high In content stripes is (24.87 ± 0.31)%, whereas in the region between the stripes it is (14.98 ± 0.10) %, yielding a ratio between 1.63 and 1.69. We note that the In-rich stripes run parallel to ridges in the overall QW morphology. Fig. 4(d) illustrates the SFs detected within the lower half of the sample. The yellow iso-concentration surfaces highlight the SF planes, revealing their parallel orientation and an approximate separation of 10 nm from one another. Looking at the Ga concentration profile below, we can see that the observed Ga concentration decreases at the locations where the field strength increases. As in the case of Fig. 3, Ga with different stoichiometric ratios is observed in GaN of uniform composition, suggesting that the structural changes associated with the presence of SFs in the sample leads to local field variations, resulting in the observed variations in Ga concentration.

It should be noted that the SFs observed in this APT data set do not appear to intersect the QWs, so that this dataset does not provide a direct insight into the compositional variations which SFs cause in InGaN QWs. However, we do observe stripes of In-rich material, not linked to obvious SF features, which is somewhat unexpected. The previous analysis by Ding et al. suggested that In-rich QWires may form adjacent to SFs and may cause the emission from the InGaN QW to exhibit a high degree of polarisation. Here, we indeed observe elongated In-rich QWires, but they do not appear to be associated with SFs. There are two possible explanations for this phenomenon. Firstly, In-rich QWires may form not only at SFs, but also at other locations. For example, the surfaces of the GaN surfaces on which the InGaN QWs are grown present elongated striations [48], and the resulting changes of surface orientation may lead to changes in In incorporation. Hence, QWires may be more prevalent in the sample than expected. (This idea is supported by the fact that the In-rich stripes run parallel to the ridges in the QW morphology, as noted above). Alternatively, there may be additional SFs in the sample which have not been picked up by our analysis of the apparent Ga-content variations. The zb-GaN contains both bunches of SFs and isolated SFs [34]. It is possible that bunches of SFs lead to larger disturbances to the surface field and more pronounced variations in stoichiometry, whereas isolated SFs have a lesser impact and are not necessarily detectable in APT. This point requires further investigation.

Meanwhile, our investigation of compositional changes along SFs also reveals their impact on elemental distribution within the Al layer. As is highlighted by crossed red dashed lines in Fig. 5(a), we can identify regions of reduced Ga content in the GaN cap above the AlGaN layer that we can tentatively identify as SFs, and some of these SFs run through the AlGaN layer. The iso-surface of the Al in the AlGaN layer (drawn at 5.5 at %) shows the variations in Al content associated with the SF locations. The examination of the site fraction distribution plots for Al and Ga from a top-down perspective in Fig. 5(b) again exhibit parallel stripes along which the composition changes, here with enrichment of the Al content, which mirrors the behaviour observed with In in the QW, as depicted in earlier results. The same trend can also be found in Fig. 5(c), where the Al content shows an increase in the region with the suggested SFs while Ga content drops. To show the effect of SF more clearly, the Al and Ga site fraction variation curves through the SFs are made in the direction of the red arrow in the volume labelled in Fig. 5(c) (Cross-sectional dimensions of 40 nm by 40 nm, bin size 0.5 nm). In Fig. 5(d), the site fraction variation of Al and Ga is evident in this region, with a notable decrease in the site fraction of Ga and a significant increase in Al at the SFs.

The average Al site fractions (Al/Al+Ga) have been calculated to determine the Al site fractions at and away from the SFs. According to the one-dimensional site fraction profiles along the direction of the perpendicular SF plane in Fig. 5(d), the near-SF site fraction was obtained by averaging the width within 3 nm of the SF centre, while the site fraction away from the SF was calculated by averaging the volume within the 5 nm to 8 nm width from the SF centre. The near-SF Al site fraction was found to be (17.34 ± 0.66)%, and the Al site fraction away from the SF was (10.28 ± 0.27)%, resulting in a ratio of 1.58 to 1.80. It should be noted that changes in field strength may affect the measured

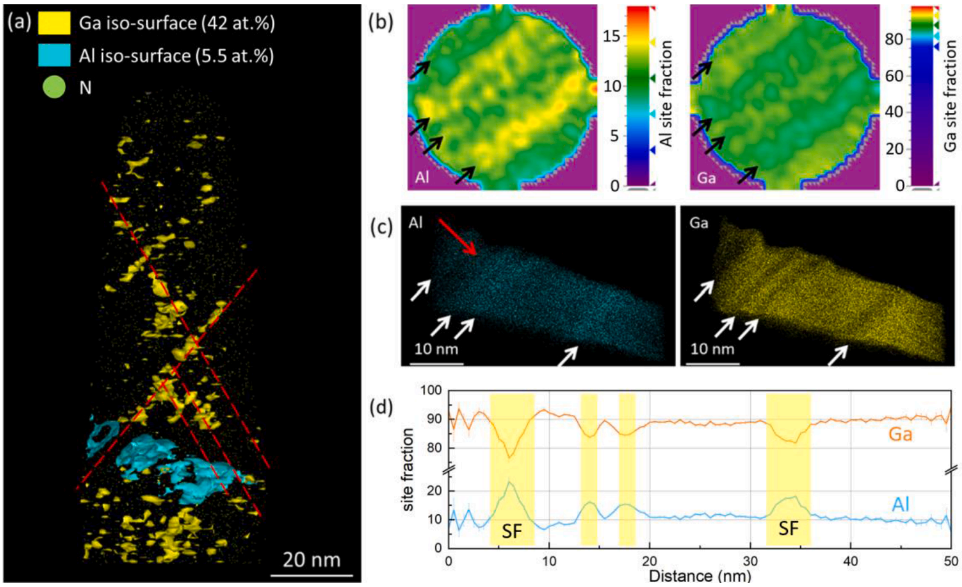

Fig. 5. (a) The portion of APT reconstruction of the dataset in Fig. 2 that includes the AlGaN layer. The red dashed lines indicate the region affected by the SFs. (b) 2D site fraction maps of Al and Ga from top view. The black arrows indicate the regions through which the SFs pass. (c) The atom maps of Al and Ga, respectively. The white arrows represent the direction of SFs. (d) Site fraction profile of Al and Ga through the AlGaN layer, perpendicular to the SF plane with the SF plane as the datum. Yellow shaded area corresponds to the SF region.

composition. A higher field at SF may lead to artificially Al-rich result [39]. However, these results correlate with earlier findings in STEM [22], suggesting that this is not entirely an artefact.

The results indicate that Al in the EBL is likely to enrich in the region of the SF compared to the SF-free region. We do not currently achieve sufficient resolution to distinguish whether the Al is segregating on the SF or in the region immediately adjacent to it, but note that previous STEM studies suggest that the AlGaN segregates directly on the SF [22]. Meanwhile, it is worth noting that multiple neighbouring SFs can interfere with each other, affecting the extent of enrichment. Further studies are needed to assess the impact of these interactions on the measured concentrations.

Lastly, we will briefly discuss potential reasons for alloy segregation in the SF region, noting that these issues are discussed in more detail in [22]. The SF can be considered as an extremely narrow insertion of wz material into the zb matrix. Bulk zincblende GaN has a larger interplanar spacing between the close packed planes than bulk wurtzite GaN. (The relevant spacings are $d_{(111)}$ in zincblende, which is 2.602 Å, and $d_{(0001)}$ in wurtzite, which is 2.593 Å) [22]. Hence, at the SF, the local interplanar spacing may be slightly reduced. Given that Al is a smaller atom than Ga, the strain associated with the presence of Al in the lattice might be reduced if Al segregates to such regions of lower interplanar spacing, reducing the total system energy.

4. Conclusions

This study presents the successful characterisation of the stacking fault (SF) structure in GaN using Scanning Transmission Electron Microscopy (STEM) and Atom Probe Tomography (APT) to provide quantitative structural and compositional information, respectively. The results show that the presence of SF (or possibly SF bunches) can be observed in both STEM and the APT reconstruction model. In terms of APT imaging, this is due to the structural changes at SF that cause changes in the evaporation field, leading to inhomogeneity in the observed Ga concentration. The presence of the SF leads to segregation of aluminium (Al) where the SF and the AlGaN layer intersect. The indium (In) distribution in the QW layers exhibits similar features. However, since there is no direct evidence in the current dataset that this is caused by SFs, further study will be needed to determine the origin of these In-rich bands or to confirm whether all SFs within the sample have been identified by APT.

In this study, APT demonstrates promising capabilities for the three-dimensional characterisation of SFs in zincblende (zb) GaN, complementing STEM. However, investigating the structural effects of SFs on different regions of the material as well as compositional variations is still a complex task. The accuracy of the structural analysis is closely related to the way the 3D reconstruction is performed, while the precision of the compositional measurements is closely related to the electric field. Future work will further explore the number and orientation of SFs and the enrichment of nearby Group III elements, as well as their relationship to the structures' optical properties.

CRediT authorship contribution statement

Ruiying Shu: Writing – original draft, Visualization, Validation, Software, Project administration, Methodology, Investigation, Formal analysis, Data curation, Conceptualization. **Rachel A. Oliver:** Writing – review & editing, Validation, Supervision, Resources, Funding acquisition. **Martin Frentrup:** Writing – review & editing, Visualization, Validation, Supervision, Software, Investigation. **Menno J. Kappers:** Writing – review & editing, Validation, Supervision. **Huixin Xiu:** Writing – review & editing, Visualization, Software, Investigation. **Gunnar Kusch:** Writing – review & editing, Supervision. **David J. Wallis:** Writing – review & editing, Supervision, Funding acquisition. **Christina Hofer:** Writing – review & editing, Validation, Supervision. **Paul A.J. Bagot:** Writing – review & editing, Validation, Supervision, Resources, Funding acquisition. **Michael P. Moody:** Writing – review & editing, Validation, Supervision, Resources, Project administration, Funding acquisition, Conceptualization.

Declaration of competing interest

The authors declare that they have no known competing financial interests or personal relationships that could have appeared to influence the work reported in this paper.

Acknowledgments

For the purpose of Open Access, the author has applied a CC BY public copyright license to any Author Accepted Manuscript (AAM) version arising from this submission. The authors gratefully acknowledge support from the Engineering and Physical Sciences Research Council (EPSRC) under the following grants: EP/S021663/1: Support for the Oxford Atom Probe Group and access to the LEAP XS atomic-scale characterisation facility. EP/R010145/1: Support for the characterisation facilities at the David Cockayne Centre for Electron Microscopy, Department of Materials, University of Oxford, and additional funding through the Henry Royce Institute. EP/W03557X/1, EP/Y004213/1, EP/R01146X/1: Support for sample growth and STEM characterisation. The authors also acknowledge support from the BEIS Energy Entrepreneurs Fund 6 for sample growth.

Supplementary materials

Supplementary material associated with this article can be found, in the online version, at doi:10.1016/j.mtla.2025.102417.

References

[1] M. Kneissl, et al., The emergence and prospects of deep-ultraviolet light-emitting diode technologies, Nat. Photonics 13 (4) (2019) 233–244.

[2] S. Huang, et al., Ultra-broadband green-emitting phosphors without cyan gap based on double-heterovalent substitution strategy for full-spectrum WLED lighting, Laser Photon. Rev. 16 (12) (2022) 2200473.

[3] J.J. Wierer Jr., J.Y. Tsao, D.S. Sizov, Comparison between blue lasers and light-emitting diodes for future solid-state lighting, Laser Photon. Rev. 7 (6) (2013) 963–993.

[4] T.D. Moustakas, R. Paiella, Optoelectronic device physics and technology of nitride semiconductors from the UV to the terahertz, Rep. Prog. Phys. 80 (10) (2017) 106501.

[5] Y. Narukawa, et al., White light emitting diodes with super-high luminous efficacy, J. Phys. D Appl. Phys. 43 (35) (2010) 354002.

[6] J. Lee, et al., Photonic crystal phosphors integrated on a blue LED chip for efficient white light generation, Adv. Mater. 30 (3) (2018) 1703506.

[7] M. Sheen, et al., Highly efficient blue InGaN nanoscale light-emitting diodes, Nature 608 (7921) (2022) 56–61.

[8] T. Mukai, M. Yamada, S. Nakamura, Characteristics of InGaN-based UV/blue/green/amber/red light-emitting diodes, Jpn. J. Appl. Phys. 38 (7R) (1999) 3976.

[9] M.R. Krames, et al., Status and future of high-power light-emitting diodes for solid-state lighting, J. Disp. Technol. 3 (2) (2007) 160–175.

[10] Y. Zhao, et al., Green semipolar (2021) InGaN light-emitting diodes with small wavelength shift and narrow spectral linewidth, Appl. Phys. Express 6 (6) (2013) 062102.

[11] Y. Jiang, et al., Realization of high-luminous-efficiency InGaN light-emitting diodes in the “green gap” range, Sci. Rep. 5 (1) (2015) 1–7.

[12] C. Humphreys, et al., The atomic structure of polar and non-polar InGaN quantum wells and the green gap problem, Ultramicroscopy 176 (2017) 93–98.

[13] H. Hu, et al., Effect of strain relaxation on performance of InGaN/GaN green LEDs grown on 4-inch sapphire substrate with sputtered AlN nucleation layer, Sci. Rep. 9 (1) (2019) 3447.

[14] C. Zhang, et al., Improvement in quantum efficiency of green GaN-based micro-LED by trapezoidal quantum well, J. Lumin. 263 (2023) 120027.

[15] Y. Huang, et al., Mini-LED, Micro-LED and OLED displays: present status and future perspectives, Light Sci. Appl. 9 (1) (2020) 105.

[16] A.R. Anwar, et al., Recent progress in micro-LED-based display technologies, Laser Photon. Rev. 16 (6) (2022) 2100427.

[17] D.J. Binks, et al., Cubic GaN and InGaN/GaN quantum wells, Appl. Phys. Rev. 9 (4) (2022).

[18] D.R. Elsaesser, et al., Optimizing GaInN/GaN light-emitting diode structures under piezoelectric polarization, J. Appl. Phys. 122 (11) (2017).

[19] M.F. Zscherp, et al., Overcoming the miscibility gap of GaN/InN in MBE growth of cubic in x Ga1−x N, ACS Appl. Mater. Interfaces 15 (33) (2023) 39513–39522.

[20] R. Kemper, et al., Growth of cubic GaN on nano-patterned 3C-SiC/Si (0 0 1) substrates, J. Cryst. Growth 323 (1) (2011) 84–87.
[21] S. Church, et al., Photoluminescence studies of cubic GaN epilayers, Phys. Status Solidi 254 (8) (2017) 1600733.
[22] B. Ding, et al., Alloy segregation at stacking faults in zincblende GaN heterostructures, J. Appl. Phys. 128 (14) (2020).
[23] S.A. Church, et al., Stacking fault-associated polarized surface-emitted photoluminescence from zincblende InGaN/GaN quantum wells, Appl. Phys. Lett. 117 (3) (2020).
[24] M.K. Miller, et al., The Local Electrode Atom Probe, Springer, 2014.
[25] M.K. Miller, et al., The future of atom probe tomography, Mater. Today 15 (4) (2012) 158–165.
[26] S.E. Bennett, et al., Atom probe tomography assessment of the impact of electron beam exposure on InxGa1−xN/GaN quantum wells, Appl. Phys. Lett. 99 (2) (2011).
[27] J.T. Griffiths, et al., The microstructure of non-polar a-plane (112¯0) InGaN quantum wells, J. Appl. Phys. 119 (17) (2016).
[28] F. Tang, et al., Nanoscale structural and chemical analysis of F-implanted enhancement-mode InAlN/GaN heterostructure field effect transistors, J. Appl. Phys. 123 (2) (2018).
[29] F. Tang, et al., Insight into the impact of atomic- and nano-scale indium distributions on the optical properties of InGaN/GaN quantum well structures grown on m-plane freestanding GaN substrates, J. Appl. Phys. 125 (22) (2019).
[30] S. Usami, et al., Direct evidence of Mg diffusion through threading mixed dislocations in GaN p–n diodes and its effect on reverse leakage current, Appl. Phys. Lett. 114 (23) (2019).
[31] P. Vacek, et al., Defect structures in (001) zincblende GaN/3C-SiC nucleation layers, J. Appl. Phys. 129 (15) (2021).
[32] L. Mancini, et al., Multi-microscopy study of the influence of stacking faults and three-dimensional in distribution on the optical properties of m-plane InGaN quantum wells grown on microwire sidewalls, Appl. Phys. Lett. 108 (4) (2016).
[33] B. Ding, et al., Multimicroscopy of cross-section zincblende GaN LED heterostructure, J. Appl. Phys. 130 (11) (2021).
[34] L.Y. Lee, et al., Investigation of stacking faults in MOVPE-grown zincblende GaN by XRD and TEM, J. Appl. Phys. 125 (10) (2019).
[35] H. Xiu, et al., Polarity determination of crystal defects in zincblende GaN by aberration-corrected electron microscopy, J. Appl. Phys. 133 (10) (2023).
[36] R. Barabash, et al., Mapping strain gradients in the FIB-structured InGaN/GaN multilayered films with 3D X-ray microbeam, Mater. Sci. Eng. A 528 (1) (2010) 52–57.
[37] R. Agrawal, et al., Characterizing atomic composition and dopant distribution in wide band gap semiconductor nanowires using laser-assisted atom probe tomography, J. Phys. Chem. C 115 (36) (2011) 17688–17694.
[38] L. Mancini, et al., Composition of wide bandgap semiconductor materials and nanostructures measured by atom probe tomography and its dependence on the surface electric field, J. Phys. Chem. C 118 (41) (2014) 24136–24151.
[39] L. Rigutti, et al., Statistical correction of atom probe tomography data of semiconductor alloys combined with optical spectroscopy: the case of Al0. 25Ga0. 75N, J. Appl. Phys. 119 (10) (2016).
[40] E. Di Russo, et al., Compositional accuracy of atom probe tomography measurements in GaN: impact of experimental parameters and multiple evaporation events, Ultramicroscopy 187 (2018) 126–134.
[41] R. Morris, et al., Toward accurate composition analysis of GaN and AlGaN using atom probe tomography, J. Vac. Sci. Technol. B 36 (3) (2018).
[42] B. Gault, et al., Behavior of molecules and molecular ions near a field emitter, New. J. Phys. 18 (3) (2016) 033031.
[43] A. Devaraj, et al., Role of photoexcitation and field ionization in the measurement of accurate oxide stoichiometry by laser-assisted atom probe tomography, J. Phys. Chem. Lett. 4 (6) (2013) 993–998.
[44] D.R. Kingham, The post-ionization of field evaporated ions: a theoretical explanation of multiple charge states, Surf. Sci. 116 (2) (1982) 273–301.
[45] B. Gault, et al., Atom Probe Microscopy, 160, Springer Science & Business Media, 2012.
[46] J.R. Riley, et al., On the reliable analysis of indium mole fraction within InxGa1−xN quantum wells using atom probe tomography, Appl. Phys. Lett. 104 (15) (2014).
[47] E. Di Russo, et al., Compositional accuracy in atom probe tomography analyses performed on III-N light emitting diodes, J. Appl. Phys. 126 (12) (2019).
[48] L.Y. Lee, et al., Effect of growth temperature and V/III-ratio on the surface morphology of MOVPE-grown cubic zincblende GaN, J. Appl. Phys. 124 (10) (2018).